Carbon 183 (2021) 929–939

Contents lists available at ScienceDirect

Carbon

journal homepage: www.elsevier.com/locate/carbon

Research Article

Sustainable paper templated ultrathin, light-weight and flexible niobium carbide based films against electromagnetic interference

Minghang Li [a, b, 1], Nan Chai [c, 1], Xingmin Liu [a, c, *], Wenjie Xie [c], Guohong Wang [a], Fangmu Qu [c], Yongchao Chen [c], Xiaomeng Fan [b], Anke Weidenkaff [c], Ralf Riedel [b, c]

[a] State Key Laboratory of Solidification Processing, Northwestern Polytechnical University, Xi'an, 710072, China
[b] Science and Technology on Thermostructural Composite Materials Laboratory, Northwestern Polytechnical University, Xi'an, 710072, China
[c] Institut für Materialwissenschaft, Technische Universität Darmstadt, D-64287, Darmstadt, Germany

ARTICLE INFO

Article history:
Received 8 April 2021
Received in revised form
14 July 2021
Accepted 18 July 2021
Available online 27 July 2021

Keywords:
Paper template
Niobium carbide
Flexible
Electromagnetic shielding

ABSTRACT

A novel and sustainable paper template-based method was developed for the fabrication of advanced niobium carbide (NbC)-based free-standing films for electromagnetic interference (EMI) shielding application. Through employing the porous structure of paper template, the simultaneous optimization of thickness, flexibility, density and shielding effectiveness (SE) of NbC-based films was facilely achieved. The pyrolytic carbon (PyC) derived from paper worked as a carbon source for the growth of the NbC phase. A hierarchically porous structure with a porosity of ~80 vol % was established to optimize the flexibility and density of the resultant films. Adjusted heterogeneous NbC-PyC nano-interfaces were formed by controlling the amount of NbC and the remaining PyC phase in the films, which significantly improved the absorption capability of EM waves. At the highest NbC content, the film possesses shielding effectiveness of 50 and 86 dB when the sample thickness is ~55 and ~220 μm, respectively compared to 32 dB of pristine paper-derived PyC film (~55 μm). These results provide guidance to explore more eco-friendly and commercially effective routes for the recycling of used paper through developing their application in the EM field.

1. Introduction

The ever-fast proliferation of compact mobile electronics and telecommunication devices has led to serious electromagnetic interference (EMI) [1–5]. EMI could not only lead to the malfunction of electronic devices but also affect the health of living organisms. To combat the EMI, electromagnetic shielding materials possessing attractive features including easy processability, light-weight, minimal thickness, as well as excellent shielding effectiveness (SE) are becoming increasingly competitive [3,4]. Besides these aforementioned features, outstanding chemical and thermal stability are also required for the engineering application of the final products [6,7]. Carbon-based nanomaterials, including graphene, carbon nanotubes and their derivatives, have been extensively used as absorbents of electromagnetic shielding materials due to the intrinsic advantageous properties including outstanding theoretical electrical conductivity, large specific surface area or aspect ratio and ultra-strong mechanical strength [8–12]. However, these materials can barely meet the aforementioned requirements in the engineering application due to challenging complexity in achieving their theoretical properties [13].

In recent years, MXenes have been widely used as building blocks of electromagnetic shielding materials owning to the large surface area, metallic conductivity, and easy aqueous processability [14–21]. In 2016, F. Shahzad et al. investigated the SE of $Ti_3C_2T_x$-based free-standing films, demonstrating outstanding EMI SE at minimal thickness [21]. Very recently, Iqbal et al. reported the SE of Ti_3CNT_x MXene based film. Results showed that the Ti_3CNT_x MXene free-standing film after annealing at 350 °C exhibits an unprecedented high SE of 116 dB (sample thickness ~40 μm), which is far better than that of other synthetic materials with comparable thickness [13]. Although MXenes have been praised for their outstanding electromagnetic property, an insurmountable challenge has been limiting both the science and applications of these materials, which is that MXenes are prone to oxidation, resulting in

* Corresponding author. State Key Laboratory of Solidification Processing, Northwestern Polytechnical University, Xi'an, 710072, China.
E-mail address: liuxm@nwpu.edu.cn (X. Liu).
[1] M.H. Li and N. Chai contributed equally to this work.

https://doi.org/10.1016/j.carbon.2021.07.056
0008-6223/

the loss of both pristine nano-sheet structure and functional properties [22]. Moreover, the complicated synthesis process of MXenes, typically involving synthesis of MAX phases at high temperatures, etching of MAX phases with highly hazardous HF, exfoliation of multi-layered MXene with poisonous chemicals, makes it time and cost ineffective, and environmentally unfriendly [23–25]. Therefore, materials of other forms and species with improved features that can be facilely prepared in an effective and eco-friendly way, will have to be explored.

Cubic niobium carbide (NbC) possesses outstanding thermal/chemical stability, excellent electrical conductivity, and relatively low synthesis temperature (1100 °C) within the TMC family [26], which is expected to be a promising material in electromagnetic shielding. However, the intrinsic high hardness, stiffness and density (7.78 g/cm^3) seriously limit the processing, machining and practical application of the final products [27].

Paper, as one of the oldest inventions has been an indispensable material that supports human civilization since its invention 2000 years ago. Apart from being often a more sustainable packaging alternative, biocompatible, renewable, and partly recyclable paper also possesses numerous advantages including adjustable thickness, good flexibility and high porosity [28,29], which exhibits great potential to be the template of advanced EMI shielding materials with the aforementioned requirements. In recent decades, the increasing print and packaging industry leads to an ever-fast consumption of paper and significant accumulation of used paper. The nuisance less disposal of the used paper is a relatively complicated process, which is an extra burden for our environment and economy. Considering the advantageous features of paper and challenges in disposing of the wasted paper, if we can recycle them as a template, advanced NbC based free-standing films can be facilely prepared by infiltration of Nb precursor into used paper and followed by pyrolysis of the Nb/paper green bodies.

Thus, in this work, ultrathin, lightweight and flexible NbC based free-standing sheets/films possessing excellent EMI SE were prepared via infiltration of an Nb precursor into the paper template, followed by pyrolysis of the Nb/paper green bodies at a temperature of 1100 °C in a protective atmosphere. Through varying the contents of Nb in the paper template, the NbC nanophase content in the resultant film, density, microstructure, electrical property and shielding effectiveness of the free-standing films were optimized. The as-prepared NbC based free-standing films were systematically investigated with respect to the phase composition, structure, electrical conductivity and EM property.

2. Experimental part

2.1. Materials synthesis

Paper pieces with a standard of 80 g/m^2 were employed as templates. Niobium chloride ($NbCl_5$) (Alfa Aesar, 99 %, metal basis) was used as the precursor to provide Nb ions. To start with, $NbCl_5$ powders were dissolved in anhydrous ethanol (Alfa Aesar, 90 wt% ethanol, 5 wt% methanol and 5 wt% isopropanol) to form a faint yellow solution. After stirring with magnetic force for 1 h, paper pieces with 2 dimensions of 6.0 × 5.0 mm^2 were sunk into the $NbCl_5$/ethanol solution and vacuum infiltrated. After immersing in the $NbCl_5$/ethanol solution for 24 h, the $NbCl_5$/ethanol-paper pieces were dried naturally at room temperature and followed by curing at 110 °C overnight in an oven. Then the $NbCl_5$/paper piece green bodies were pyrolyzed at 1100 °C in inert atmosphere (Ar). $NbCl_5$/ethanol solutions with different concentrations (0.28, 0.37, 0.75 and 1.49 M) were prepared to adjust the content of NbC. According to the content of NbC, the samples were denoted as samples S-2 to S-5. For example, sample S-2 represents the material derived from the paper template immersed in the solution that Nb ions concentration amounts 0.28 M/L. A control test sample derived from the pristine paper was denoted as sample S-1.

2.2. Materials characterization

Scanning electron microscopy (SEM) (Hitachi, S-4700, 15 kV) was employed to characterize the morphology. The phase lattice and NbC-PyC nano-interface in the NbC-based film were observed with transmission electron microscopy (TEM) (FEI Tecnai, F200X, 200 kV). X-ray diffraction (XRD) (X'Pert Pro, Philips, Netherlands, Cu Kα radiation) were employed to obtain the phase composition and crystallinity. XPS (Axis Supra, Kratos, UK) were employed to characterize the bonding and element information. The BET measurement were acquired according to the results of N_2 adsorption/desorption measurement at 77 K by an Autosorb-3B Analyzer (Quantachrome Instruments Corporation). Raman spectra were recorded via a micro-Raman HR8000 spectrometer (Bensheim, Horiba JobinYvon, Germany, 514.5 nm) to obtain the crystallinity of carbon phase. The electrical property were measured by a four-pin probe method (MCP-T610 model, Mitsubishi Chemical, Japan) with a Loresta-GP meter. A vector network analyzer (VNA, Agilent Technologies E8362B) was used to characterize the S-parameters in the X-band (8.2–12.4 GHz).

3. Results and discussion

3.1. Porous NbC based free-standing film preparation

The intrinsic properties of cubic NbC including high hardness, stiffness and density have been the challenges for the processing, machining as well as practical application of NbC based films. To overcome these problems, a sustainable, novel and facile paper template combined precursor infiltration and pyrolysis method was developed in this work. Fig. 1a shows the schematic preparation process of the NbC-based free-standing film. The pristine porous structure of the paper enables the efficient infiltration of the precursor $NbCl_5$/ethanol solution. The cellulose in the fibers of the paper acts as carbon source for the growth of NbC. After vacuum infiltration and drying, the $NbCl_5$/paper green bodies were heat-treated at the temperature of 1100 °C for 3h. Fig. 1b and c are the optical images of the paper-derived PyC film and free-standing NbC-based film. As shown in Fig. 1b, the pristine paper-derived PyC film exhibits a twisted and rough morphology. Different from the PyC film prepared under identical conditions, the NbC based free-standing film exhibits a rather flat surface. We suggest this results from the formation of this highly porous structure (Fig. 1e) during the precursor-to-ceramic conversion, allowing for the release of stress in the heating treatment process [30].

3.2. Crystalline phase and microstructure

The phase composition of synthesized materials was characterized with Raman, XRD and XPS. In Fig. 2a, Raman spectra of the paper-derived PyC film and NbC based films with varying NbC content were presented, where D-peak (~1350 cm^{-1}) resulting from the defects of carbon and G-band (~1580 cm^{-1}) related to the degree of graphitization were identified[31]. As shown in all samples, the intensity of D peak (I_D) is always larger than the intensity of G peak (I_G) due to the highly amorphous state. Interestingly, the ratios of I_D/I_G of different batches of the samples do not change obviously, which indicates an invariant degree of graphitization. In Fig. 2b, two weak peaks in between 45°-50° were observed in the XRD spectrum of pristine paper derived film. Based on the literature [32], these two peaks are the characteristic peaks of CaO

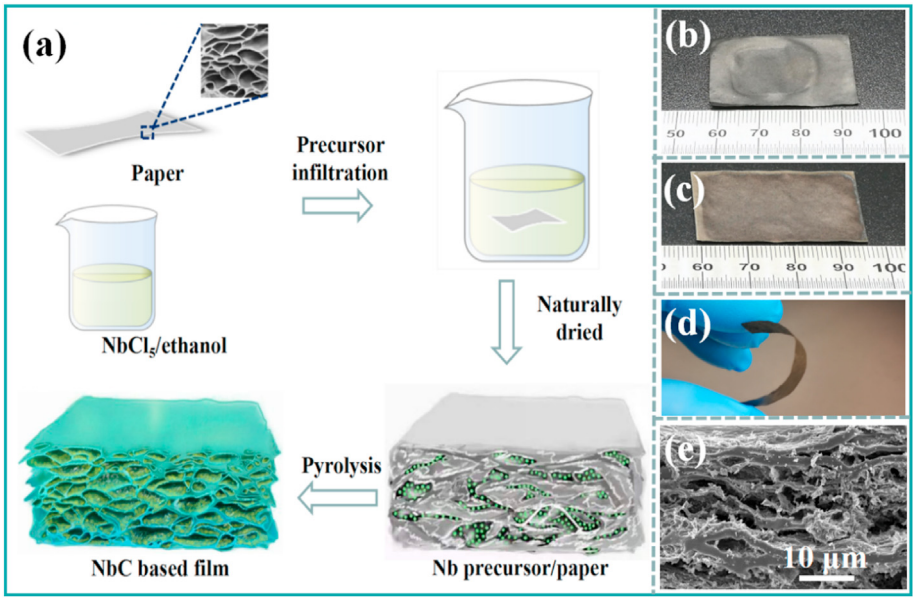

Fig. 1. a) Schematic showing on the developing procedure of NbC based film, b) and c) optical photos of PyC and NbC based films, d) optical image of NbC based film with a flexible test bending, and e) cross section morphology of the NbC-based film of SEM image. (A colour version of this figure can be viewed online.)

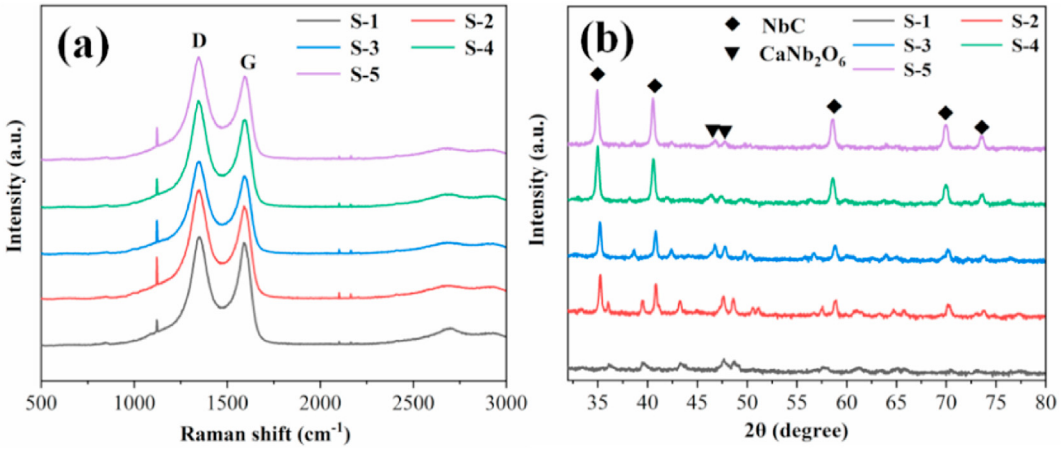

Fig. 2. a) Raman spectroscopy and b) XRD of the resulting sample powders heat treated at 1100 °C in argon atmosphere. (A colour version of this figure can be viewed online.)

derived from the decomposition of $CaCO_3$ in the pristine paper. Meanwhile, with the introduction of Nb element into the paper, these two peaks were found to shift to small angle range (S.1). We suggest this is resulted from the formation of $CaNb_2O_6$ phase in the resultant films. Moreover, five characteristic peaks corresponding to cubic NbC phase of the NbC-based films were detected. The first peak at 34.9° stems from the (1 1 1) lattice plane while these peaks located at $2\theta = 40.5°$, 58.6°, 70.0° and 73.6° are due to the lattice planes of (2 0 0), (2 2 0), (3 1 1), and (2 2 2), respectively[33,34]. The appearance of the NbC related diffractions indicates the successful formation of crystalline NbC in the resultant films. From samples S-2 to S-5, the intensity of the representative NbC peaks increased gradually, which is resulted from the increasing amount of NbC content in-situ formed in the free-standing film due to the increased amount of Nb precursor infiltrated into the paper templates.

The elemental composition of the resulting NbC-based film powder was investigated by the XPS technique (Fig. 3). In Fig. 3a, the overview of the XPS spectrum confirms the existence of C, O, Nb and Ca, respectively. Ca is detected due to the $CaCO_3$ impurity phase in the pristine paper. The peak located at 284.6 eV in the spectra of C 1s (Fig, 3b) comes from the presence of C—C bonds, proving the presence of carbon element. The peaks at 283.3 eV can be ascribed to Nb—C bond [33–35]. The peak at 288.4 eV stems from the C—*O*—C bond [30], which means that the carbon phase in the samples containing many defects, agreeing with the results in Raman. The XPS spectrum of Nb 3d state is deconvoluted to a variety of different oxidation states of Nb, including NbC_xO_y, Nb_2O_5 and Nb_2O_3. The detection of the Nb—O is due to the oxidation of the NbC during the cooling or insufficient reaction of Nb ions/cations with the carbon source.

To get to know the morphology of the synthesized NbC-based films, the cross-sections of each batch of the films were observed with SEM. The pristine paper-derived PyC film possesses a thickness of about 60 μm after pyrolysis at 1100 °C for 3h, as shown in Fig. 5a. In Fig. 5b and c, the PyC film exhibits a porous structure with micrometer-sized rectangular pores. Based on the Archimedes methods, the open porosity of the film is calculated to be 37.5 %. The

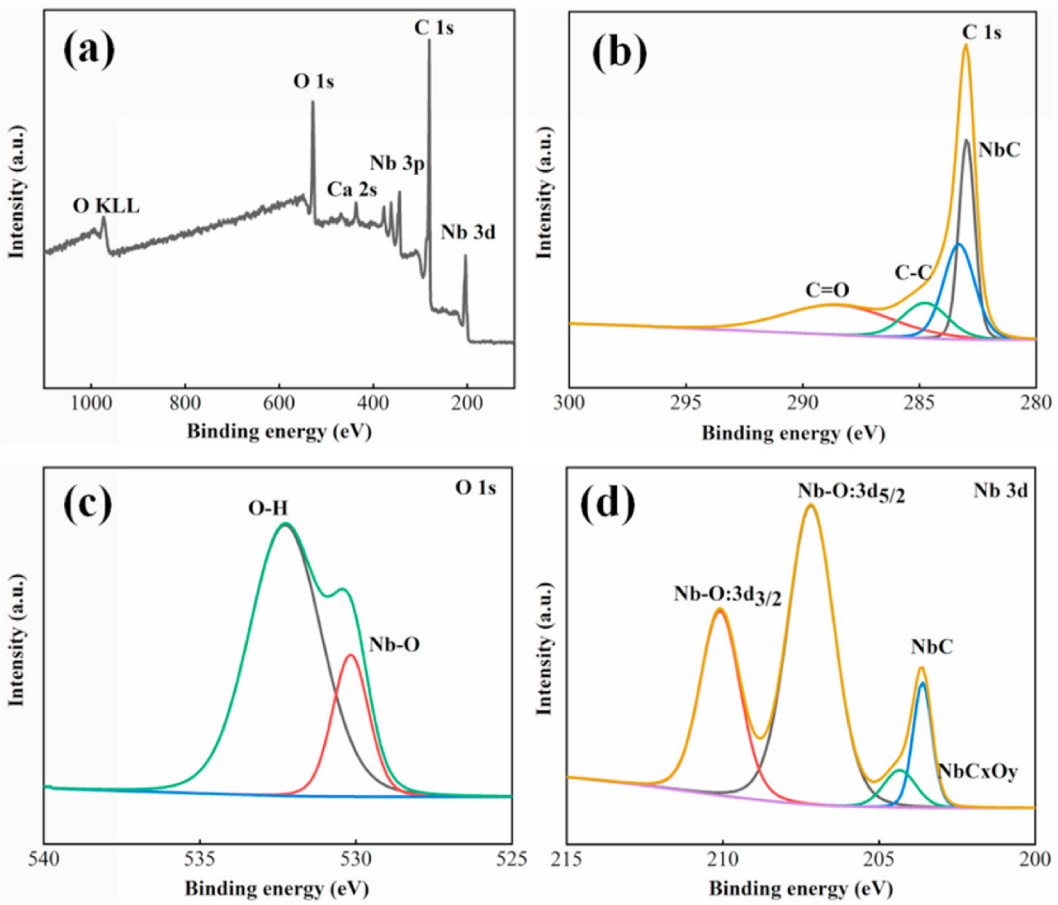

Fig. 3. a) Overview XPS spectrum of NbC-based power sample, b), c) and d) XPS spectra of C 1s, Nb 3d and O 1s. (A colour version of this figure can be viewed online.)

porous film structure is discussed in terms of a) the pristine paper possesses a porous structure and b) volume shrinkage of the cellulose fibers during the pyrolysis process [3]. Moreover, the cross-section and lateral profile of PyC fibers derived from the thermolysis of cellulose were analyzed by high magnification SEM, which forms the backbone of the film. With the formation of NbC, the thickness of the films did not change (Fig. 4d). However, from the high magnification SEM images (Fig. 4e and f), the formation of a highly porous and multi-layered structure was visible. As calculated, with the introduction of NbC, the open porosity in sample S-2 reached values as high as 79 vol%, which amounted to almost two times of control test sample. The highly porous and hierarchical structure is considered to be formed due to the fast generation of large amounts of gaseous byproducts during pyrolysis. In the presence of $NbCl_5$, corrosive and/or gaseous byproducts such as HCl or Cl_2 were formed, leading to a fast decomposition of the cellulose. Furthermore, accumulation of gaseous byproducts in closed pores led to stress concentration and thus resulted in the propagation of cracks and expansion of closed pores. The formation of successive pores allows for the deformation of the sub-layers under pressure and enhances flexibility of the films[30]. With further increase of the NbC content, the open porosity did not change significantly and varies between 75 and 80 vol%. With increasing concentration of $NbCl_5$/ethanol solution, particles with a bright contrast in SEM are found to form inside the films (Fig. 4i, l and 4°). Based on the XRD results, these particles were analyzed to be the NbC phase. Owning to the better electrical property of NbC[3,36,37], a brighter contrast of the NbC particles than that of the PyC substrate was observed in SEM images. With the increasing precursor concentration, the amount of NbC increased accordingly (S-3, S-4 and S-5), which agrees well with the XRD results in Fig. 2a.

N_2 adsorption/desorption isotherms of samples S-1, S-3 and S-5 were measured to further analyze the porosity of the films. The isotherms of the measured samples obey the Type IV characteristic feature as shown in Fig. 5a and are, therefore, associated with the presence of mesopores. The corresponding pore volume of samples S-1, S-3 and S-5 are 0.33, 0.51 and 0.50 cm^3/g, indicating the increase of open porosity with the formation of NbC nanophase in the film. From Fig. 5b we can see that the pore size of samples S-1, S-3, and S-5 mainly varies between 3 and 50 nm, the typical range of mesopores. Moreover, with the increasing NbC content, the amount of mesopores increases accordingly.

To analyze the particle size and structure of the NbC phase, TEM studies of samples (S-3) were conducted (Fig. 6). The particles exhibit a highly porous structure, where mesopores with diameters between 10 and 50 nm are identified (Fig. 6a). In the matrix, NbC particles with different diameters were found. Some remaining PyC phase was also visible in higher resolution TEM image in Fig. 6b. Annular gaps between NbC and PyC with diameters of lower than 10 nm were also detected. The TEM images also support the measured BET results and agree with the presence of mesopores. Moreover, a heterogeneous interface between crystalline NbC and the PyC phase was detected (Fig. 6c and d). The presence of these interfaces is considered to improve the polarization loss and thus will lead to the improvement of the shielding by absorption. Clear lattice fringes can be observed on the edge of the NbC phase, where

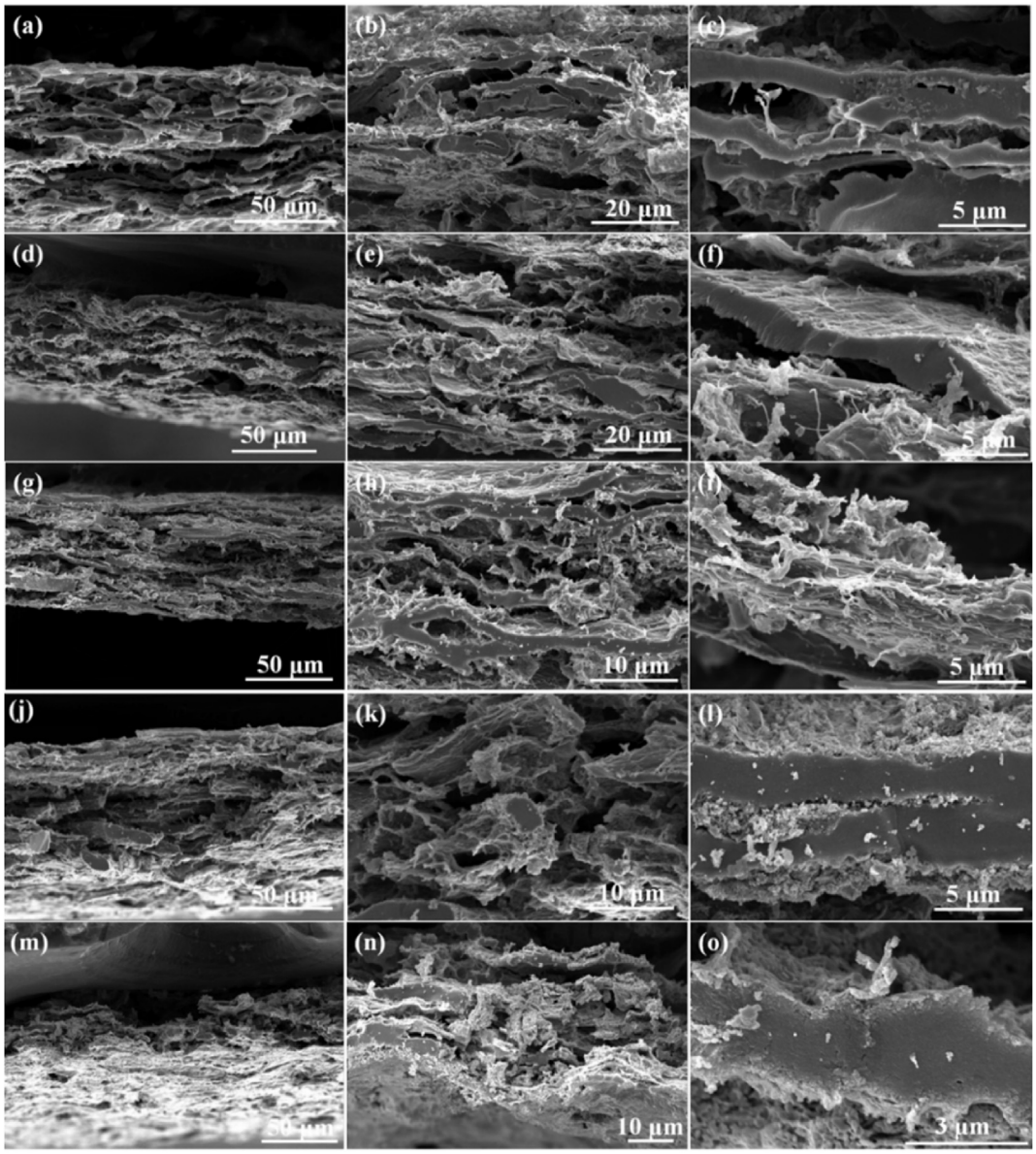

Fig. 4. a), b) and c) cross section morphology of pristine paper derived PyC film (S-1), d), e) and f) cross section morphology of sample S-2, g), h) and i) cross section morphology of sample S-3, j), k) and l) cross section morphology of sample S-4, m), n) and o) cross section morphology of sample S-5, with varied magnification.

the interface between the PyC and NbC is further enlarged. In Fig. 6e–i, EDS technique was used to confirm the elements and location in the resulting film. From Fig. 6f–i, C, Nb, O and Ca are detected in the powder materials, where the Ca is stems from $CaCO_3$ in the pristine paper.

3.3. Electrical conductivity

In the electromagnetic shielding, electrical conductivity is not the necessity for the high efficient EM shielding performance [38,39]. However, an improved electrical conductivity leads to an enhanced EMI SE [40–42].

As observed from the SEM images, the NbC/PyC backbone sub-layers are geometrically parallel, rather than vertical to the in-plane directions of the films. When the electromagnetic waves are incident into the films, the NbC/PyC backbone sub-layers parallel to the in-plane directions work as shields and block the EM waves from transmitting. So, in this work, the in-plane electrical conductivity of all batches of samples were provided (Fig. 7). Due to the significant increase of the open porosity from 37.5 % (sample S-1) to 79 % (sample S-2), the electrical conductivity exhibited a significant decrease from 41.3 S/cm to 18.7 S/cm. However, with the increasing NbC content in the free-standing films, the electrical conductivity increases, which results from the co-influence of porosity, intrinsic electrical conductivity and volume percentage of each phase [43–45]. To address the relationship, many empirical equations have been proposed in the literature [43–45], which takes pore size, porosity and shape of pores into consideration. Here, a critical and comprehensive formula which combines the percolation theory and effective medium approximation, is expressed as [44].

$$\sigma = \sigma_0 (1 - \frac{P}{P_c})^x \quad (1)$$

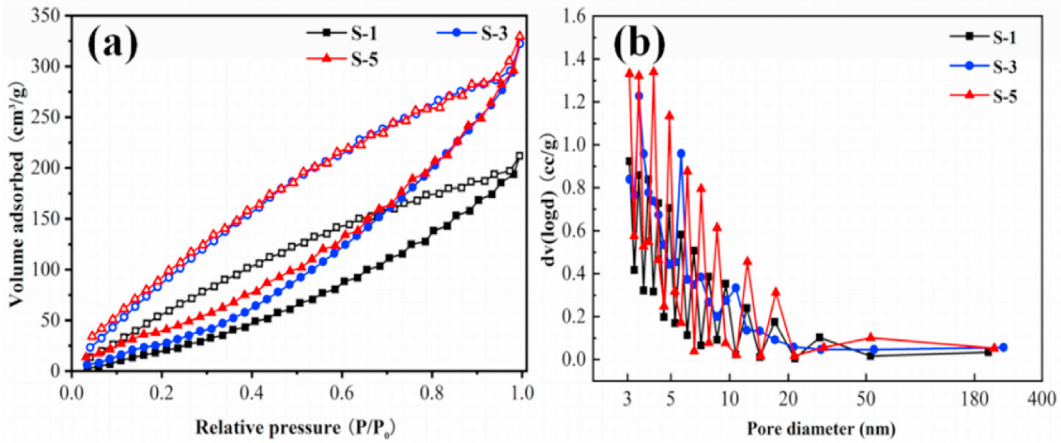

Fig. 5. a) N_2 adsorption/desorption isotherms of S-1, S-3, and S-5; b) distributions of the pore size in samples S-1, S-3, and S-5. (A colour version of this figure can be viewed online.)

Where x is a critical exponent, and P_c is the critical porosity. Theoretically, this equation can describe the electrical conductivity dependence of porosity from low porosity range to high porosity range, even higher than 50 %. For multi-phase materials, the equation should be modified as [45].

$$\sigma = \sum_{n=1}^{n} \sigma_i v_i (1 - \frac{P}{P_c})^x \quad (2)$$

$$\sigma_0 = \sum_{n=1}^{n} \sigma_i V_i \quad (3)$$

Where n represents the number of phases, σ_i and V_i represent the theoretical electrical conductivity and volume percentage of the individual phase.

Based on the literature [43–45], the decrease of electrical conductivity results from the significant increase of the porosity. With the same porosity level (samples S-2 to S-5), we suggest the electrical conductivity is dominated by the volume percentage of the NbC phase. So, the electrical conductivity increased with the increasing NbC content, which reached 37.2 S/cm at the largest NbC content in this work. Increasing electrical conductivity is attributed to the increasing amount of electrons from the better conductive NbC phase. However, it is still not as high as that of the PyC film because of the large open porosity in the NbC based films.

3.4. Electromagnetic shielding mechanism and effectiveness

The efficiency of materials to hinder the propagation of EM waves is denoted as shielding effectiveness (*SE*)[8,46,47]. As mentioned in the literature and our former work [48–51], reflection SE (SE_R), multiple reflection SE (SE_{MR}) and absorption SE (SE_A) and are the main shielding mechanisms contributing to the total shielding effectiveness (SE_T). Multiple reflections typically result from reflections at the internal surfaces of the shields. Skin depth (δ) is the distance where the current density in the conductor drops to 1/e of the current density on the surface of the conductor. Based on this, the re-reflected microwaves will be dissipated inside the materials, when the SE_A is high enough ($\geq$10 dB) or the shielding materials is thicker than the δ. The contribution of SE_{MR} can be ignored in this case and the SE_T can be expressed by[4,52,53].

$$SE_T = SE_R + SE_A \quad (4)$$

The SE_R and SE_A are obtained with the following equations [53,54].

$$SE_R = -10\log(1-R) \quad (5)$$

$$SE_A = -10\log(T/(1-R)) \quad (6)$$

$$R = |S_{11}|^2 = |S_{22}|^2 \quad (7)$$

$$T = |S_{21}|^2 = |S_{12}|^2 \quad (8)$$

$$A = 1 - R - T \quad (9)$$

where *R, A, and T are* the power of reflection, power of absorption and power of transmitting, respectively.

The EMI *SE* of the paper derived PyC and NbC-based free-standing films from 8.2 to 12.4 GHz are presented (Fig. 8). In Fig. 8a, the SE_T value of the pristine paper derived PyC film reaches 32 dB at 8.2 GHz after annealing of the paper at 1100 °C for 3 h, indicating >99.9% of EM waves are attenuated. With the inclusion of NbC in the film, the SE_T value of NbC-based film was enhanced to 41 dB, which is different from the varying tendency of electrical conductivity. We suggest the increase of the SE_T results from the following reasons: (a) the increasing amount of electrons contributed by the better electrical conductive NbC phase leads to the increase of reflection capability and conductive loss; (b) the construction of NbC-PyC heterogeneous interface leads to interface polarization loss, leading to the increase of SE_A (Fig. 8b); (c) the highly porous structure enables the multi-reflection of EM waves, leading to the gradual dissipation of EM waves inside the materials. With further increasing NbC content, the SE_T constantly increases. At the largest NbC content (Sample S-5), the SE_T is as high as 50 dB when the sample thickness is ~55 μm. The significantly improved SE_T is attributed to the inclusion of highly conductive NbC in the PyC matrix. To make a comparison with the carbon-based material, commercial available grafoil with a thickness of 100 μm was employed in this work. The EMI *SE* of grafoil as a function of thickness was provided in S.2. As shown in S.2, when the thickness of grafoil is 100 and 200 μm, the mean value of EMI SE is 15 and 26 dB, while the EMI SE NbC-based film (sample S-5) can reach as high as 52 dB at the thickness of 110 μm (Fig. 9), which unambiguously indicates the excellent performance of the NbC-based films.

Material thickness is another factor that influences the electromagnetic performance of materials [21]. Fig. 9a–c show the EMI *SE* and power balance of sample S-5 as a function of the material

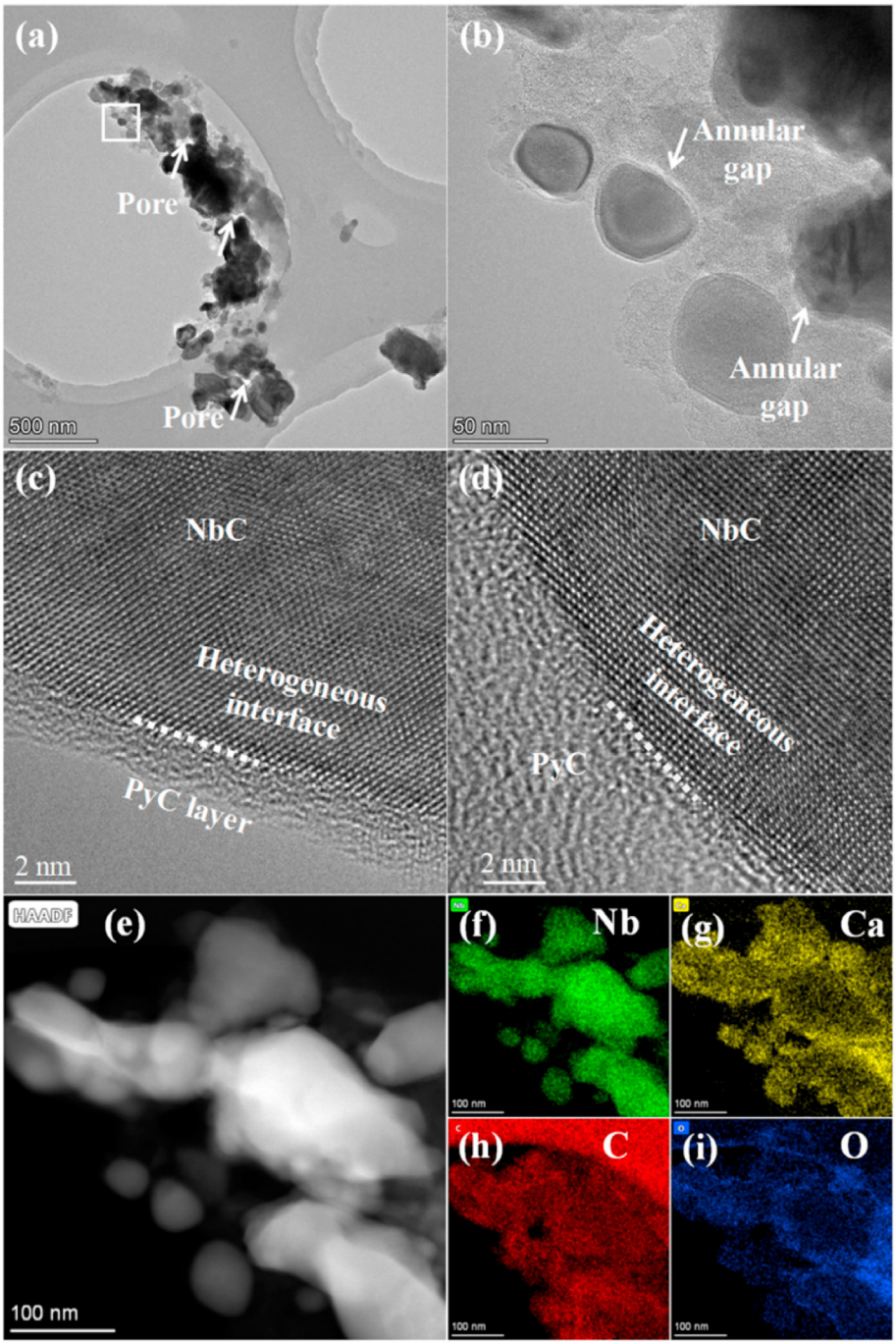

Fig. 6. a) TEM image of the NbC-based film powder, High-resolution TEM image of the b) area in circle, c) and d) NbC and interface to PyC, e) HAADF image of the NbC based film powder, f), g), h) and i)overlapped area EDX mapping of Nb, Ca, C and O. (A colour version of this figure can be viewed online.)

thickness. From Fig. 9a, we can see that the SE_T increases with the increasing material thickness. At a thickness of ~220 μm (4 layers), the EMI *SE* reaches 86 dB and the mean value in the X band amounts to 80 dB (Fig. 9b). The SE_A and SE_R of all films possess the consistent varying tendency as with the SE_T (Fig. 9b). The increased SE_A can be attributed to the construction of heterogeneous interfaces of NbC-PyC (Fig. 9d) and defects in the PyC [2,3,8] and the increasing amount of free electrons contribute to the increase of the SE_R. Based on the reported model [2,3,8], relaxation losses can contribute to EM attenuation by polarization and relaxation in materials (e.g. defects and heterogeneous nano-interface). The strong reflection power of the materials is higher than 0.96 nW and is shown in Fig. 9c. With increasing material thickness, the reflection power increases, which means that the reflection occurs not only on the surface but also on internal interfaces of the porous films.

Besides EMI SE, the density and thickness are another two attractive features to evaluate the workability in the engineering applications [21,30]. When taking them into account, the SE_T divided by bulk density and material thickness (SSE/t) is used to evaluate different materials. With the formation NbC content in the NbC-based free-standing film (Fig. 10a), the density exhibites a

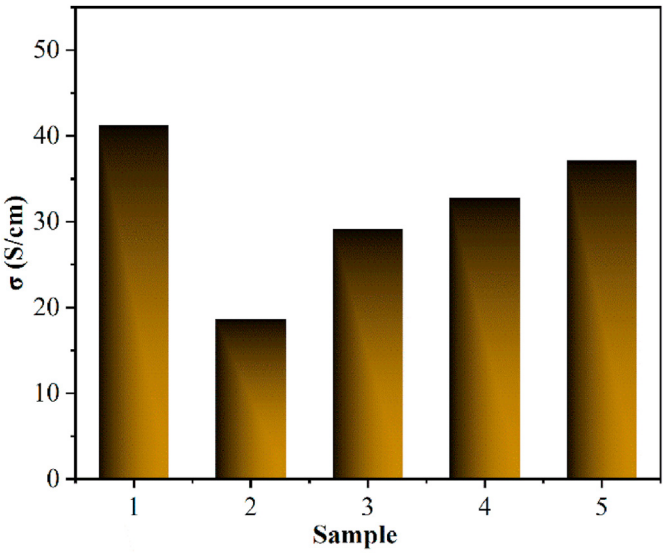

Fig. 7. Electrical conductivity of the free-standing PyC and NbC based films. (A colour version of this figure can be viewed online.)

significant decrease from 1.35 to 0.71 g/cm^3 owning to the significant increase of porosity from 37.5 to ~79.0 vol%. With the increasing amount of NbC content, the density increases gradually. At the largest NbC content, the density of the free-standing film increases to 0.75 g/cm^3, which is lower than 1/10 of the theoretical density of NbC. Among all batches of samples, the pristine paper derived PyC film exhibits the lowest *SSE/t* value (3974.1 dB.g^{-1}cm^2) due to the inferior EMI SE and larger density. With the significant increase in EMI SE and decrease in density of sample S-5, the value of *SSE/t* increased to 9380.2 dB.g^{-1}cm^2, which is competitive among other reported EMI shielding materials. Apart from that, applicable mechanical strength is also necessary in the engineering application. In this work, due to the same porosity level, the tensile strength of resultant NbC-based films exhibits similar value. In S.3, the tensile strength of a representative NbC-based film is given. As shown (S.3), the tensile strength of resultant film can reach as high as 1.5 MPa, which is about 2 orders of magnitude higher than that of the graphene-foam based materials [48]. Furthermore, stability of advanced EMI shielding materials in aggressive atmosphere (e.g, chemical and thermal) and mechanical property should also be considered in the engineering application. NbC-based materials have been well known for the outstanding performance in aggressive environments (e.g. ultra high temperature) [55,56]. Considering the length of current manuscript, mechanical strength and EMI SE in aggressive environments will have to be reported in the future work.

4. Conclusion

A sustainable and facile paper template infiltrated with an NbC precursor solution and subsequently pyrolyzed was developed for the development of light-weight and flexible NbC-based free-

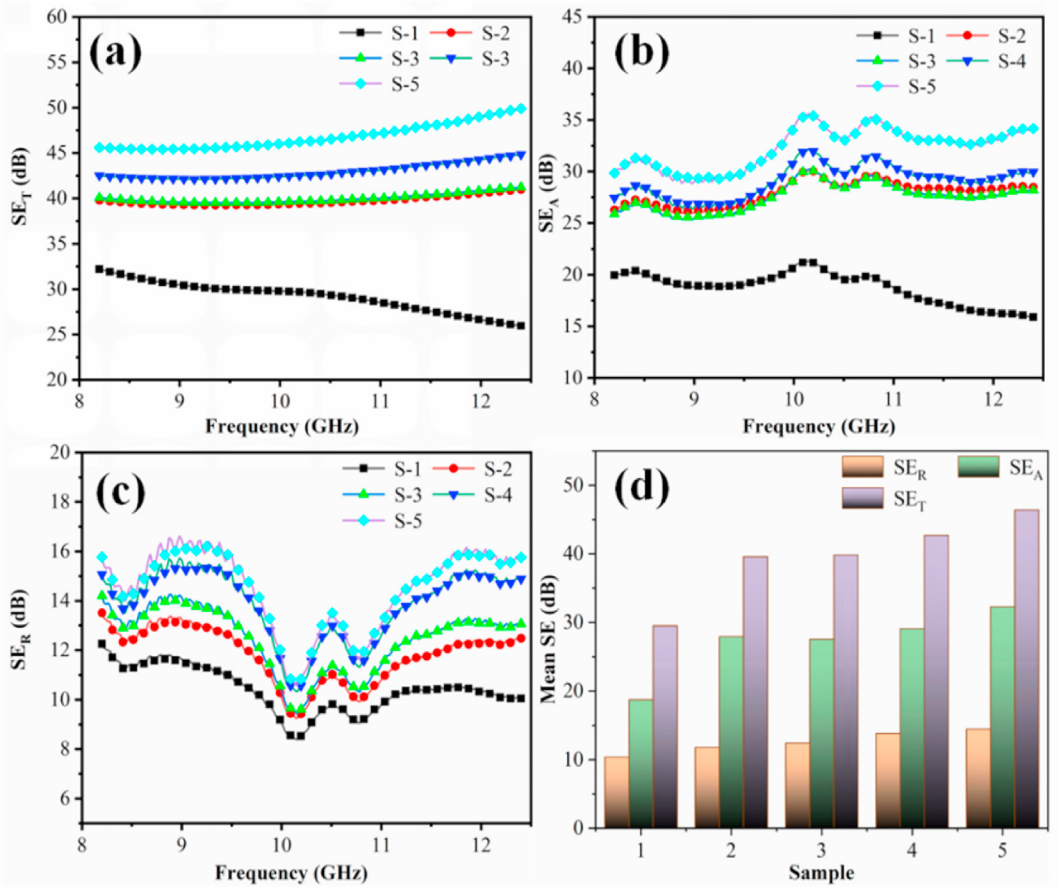

Fig. 8. a) SE_T, b) SE_A and c) SE_R of resulting materials with respect to of precursor concentration, d) Mean values in SE_T, SE_A and SE_R of the NbC-based films. (A colour version of this figure can be viewed online.)

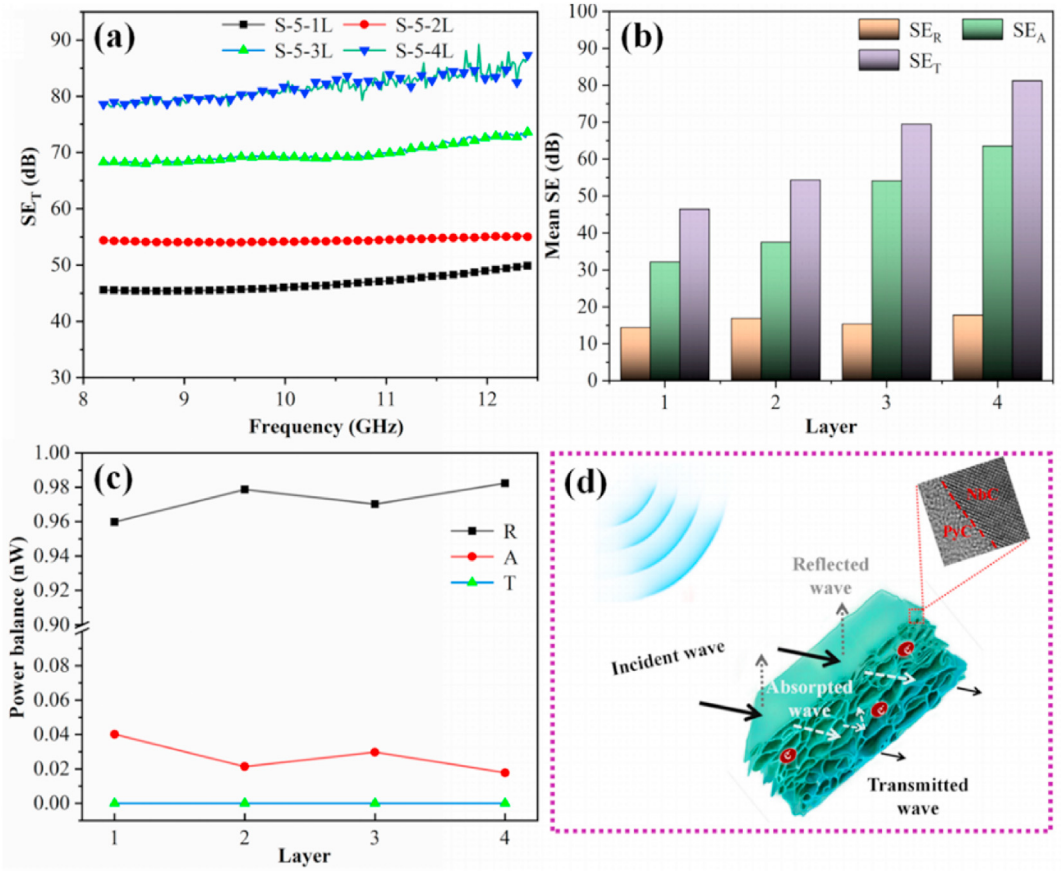

Fig. 9. a) EMI SE_T of resultant film (sample S-5) as a function of sample layers b) Mean value of shielding performance as a function of sample layers, c) Power balance of resultant materials, d) Shielding mechanism of resultant materials. (A colour version of this figure can be viewed online.)

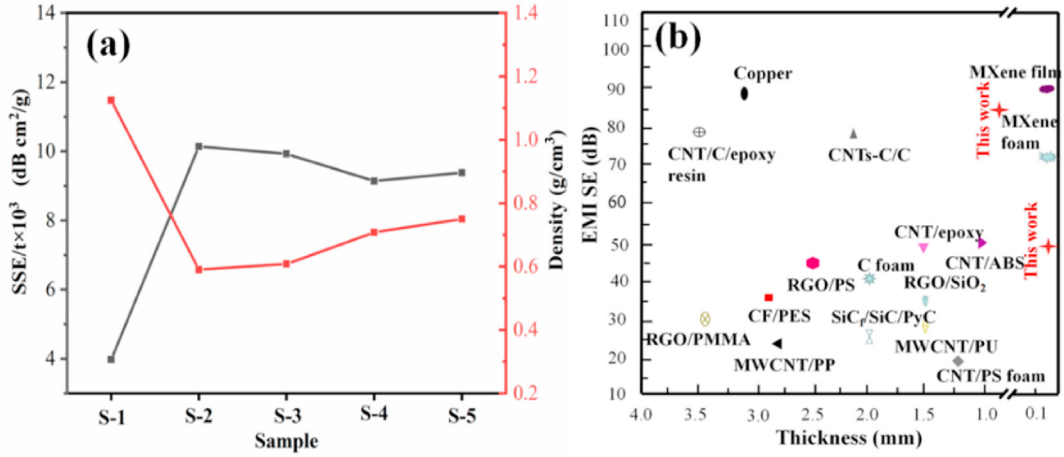

Fig. 10. a) Bulk density and *SSE/t* value of the NbC-based films, b) the EMI SE versus thickness of reported works [3,21].

standing films. The in-situ growth of the NbC nanophase in the paper templated films led to the establishment of a hierarchically porous microstructure. The synthesized films are characterized by low density and good flexibility. The final NbC content can be adjusted by controlling the Nb precursor amount inside the paper template. With the increase of NbC phase in the films, the SE of the NbC based films is greatly enhanced. When the thickness of the sample is ~55 μm, the EMI SE of the NbC-based film reaches 50 dB, significantly superior than 32 dB of the PyC film derived from pristine paper. The excellent potential of NbC in the EMI shielding field is revealed in this work and may explore a pioneering route for developing of other TMCs-based EMI shielding materials in general. Moreover, our current work find a facile approach for the application of recycled and wasted paper in an eco-friendly and economical way in form of advanced high-tech EM shielding materials.

Declaration of competing interest

The authors declare that they have no known competing financial interests or personal relationships that could have appeared to influence the work reported in this paper.

Acknowledgment

X.M. Liu acknowledge the supporting of the National Natural Science Foundation of China (No. 52002325) and the Fundamental Research Funds for the Central Universities (No. 3102019TS0405). The authors give their warm thanks for the structural characterization by the Analytical & Testing Center of NWPU.

Appendix A. Supplementary data

Supplementary data to this article can be found online at https://doi.org/10.1016/j.carbon.2021.07.056.

References

[1] L. Wang, H. Qiu, P. Song, Y. Zhang, Y. Lu, C. Liang, J. Kong, L. Chen, J. Gu, 3D Ti_3C_2Tx MXene/C hybrid foam/epoxy nanocomposites with superior electromagnetic interference shielding performances and robust mechanical properties, Composites Part A, Applied Science & Manufacturing 123 (2019) 293–300.
[2] M. Cao, C. Han, X. Wang, M. Zhang, Y. Zhang, J. Shu, H. Yang, X. Fang, J. Yuan, Graphene nanohybrids: excellent electromagnetic properties for the absorbing and shielding of electromagnetic waves, J. Mater. Chem. C 6 (17) (2018) 4586–4602.
[3] X. Liu, H. Xu, F. Xie, X. Yin, R. Riedel, Light-weight and highly flexible TaC modified PyC fiber fabrics derived from cotton fiber textile with excellent electromagnetic shielding effectiveness, Chem. Eng. J. 387 (2020) 124085–124097.
[4] H. Lv, Z. Yang, S.J.H. Ong, C. Wei, H. Liao, S. Xi, Y. Du, G. Ji, Z.J. Xu, A flexible microwave shield with tunable frequency-transmission and electromagnetic compatibility, Adv. Funct. Mater. 29 (14) (2019) 1900163–1900171.
[5] P. Song, H. Qiu, L. Wang, X. Liu, Y. Zhang, J. Zhang, J. Kong, J. Gu, Honeycomb Structural rGO-MXene/epoxy Nanocomposites for Superior Electromagnetic Interference Shielding Performance, Sustainable Materials Technologies, 2020, 00153.
[6] M. Albano, D. Micheli, G. Gradoni, R.B. Morles, M. Marchetti, F. Moglie, V.M. Primiani, Electromagnetic shielding of thermal protection system for hypersonic vehicles, Acta Astronaut. 87 (2013) 30–39.
[7] C. Liang, Z. Wang, Eggplant-derived SiC aerogels with high-performance electromagnetic wave absorption and thermal insulation properties, Chem. Eng. J. 373 (2019) 598–605.
[8] M.S. Cao, Y.Z. Cai, P. He, J.C. Shu, W.Q. Cao, J. Yuan, 2D MXenes: electromagnetic property for microwave absorption and electromagnetic interference shielding, Chem. Eng. J. 359 (2019) 1265–1302.
[9] B. Wen, M. Cao, M. Lu, W. Cao, H. Shi, J. Liu, X. Wang, H. Jin, X. Fang, W. Wang, J. Yuan, Reduced graphene oxides: light-weight and high-efficiency electromagnetic interference shielding at elevated temperatures, Adv. Mater. 26 (21) (2014) 3484–3489.
[10] H. Chen, Z. Huang, Y. Huang, Y. Zhang, Z. Ge, B. Qin, Z. Liu, Q. Shi, P. Xiao, Y. Yang, T. Zhang, Y. Chen, Synergistically assembled MWCNT/graphene foam with highly efficient microwave absorption in both C and X bands, Carbon 124 (2017) 506–514.
[11] L. Wang, X. Yu, X. Li, J. Zhang, M. Wang, R. Che, Conductive-network enhanced microwave absorption performance from carbon coated defect-rich Fe_2O_3 anchored on multi-wall carbon nanotubes, Carbon 155 (2019) 298–308.
[12] Z. Xiang, J. Xiong, B. Deng, E. Cui, L. Yu, Q. Zeng, K. Pei, R. Che, W. Lu, Rational design of 2D hierarchically laminated Fe_3O_4@ nanoporous carbon@ rGO nanocomposites with strong magnetic coupling for excellent electromagnetic absorption applications, J. Mater. Chem. C 8 (6) (2020) 2123–2134.
[13] A. Iqbal, F. Shahzad, K. Hantanasirisakul, M.K. Kim, J. Kwon, J. Hong, H. Kim, D. Kim, Y. Gogotsi, C.M. Koo, Anomalous absorption of electromagnetic waves by 2D transition metal carbonitride Ti_3CNT_x (MXene), Science 369 (6502) (2020) 446–450.
[14] M. Naguib, V.N. Mochalin, M.W. Barsoum, Y. Gogotsi, 25th anniversary article: MXenes: a new family of two-dimensional materials, Adv. Mater. 26 (2014) 992–1005.
[15] M.R. Lukatskaya, O. Mashtalir, C.E. Ren, Y. Dall'Agnese, P. Rozier, P.L. Taberna, M. Naguib, P. Simon, M.W. Barsoum, Y. Gogotsi, Cation intercalation and high volumetric capacitance of two-dimensional titanium carbide, Science 341 (2013) 1502–1505.
[16] M. Han, X. Yin, H. Wu, Z. Hou, C. Song, X. Li, L. Zhang, L. Cheng, Ti_3C_2 MXenes with modified surface for high-performance electromagnetic absorption and shielding in the X-band, ACS Appl. Mater. Interfaces 8 (32) (2016) 21011–21019.
[17] R. Sun, H. Zhang, J. Liu, X. Xie, R. Yang, Y. Li, S. Hong, Z. Yu, Highly conductive transition metal carbide/carbonitride (MXene)@polystyrene nanocomposites fabricated by electrostatic assembly for highly efficient electromagnetic interference shielding, Adv. Funct. Mater. 27 (45) (2017) 1702807.
[18] W. Cao, F. Chen, Y. Zhu, Y. Zhang, Y. Jiang, M. Ma, F. Chen, Binary strengthening and toughening of MXene/cellulose nanofiber composite paper with nacre-inspired structure and superior electromagnetic interference shielding properties, ACS Nano 12 (5) (2018) 4583–4593.
[19] C. Zhang, S. Pinilla, N. McEvoy, C.P. Cullen, B. Anasori, E. Long, S.M. Park, A. Seral-Ascaso, A. Shmeliov, D. Krishnan, C. Morant, X. Liu, G.S. Duesberg, Y. Gogotsi, V. Nicolosi, Oxidation stability of colloidal two-dimensional titanium carbides (MXenes), Chem. Mater. 29 (11) (2017) 4848–4856.
[20] J. Liu, H. Zhang, R. Sun, Y. Liu, Z. Liu, A. Zhou, Z. Yu, Hydrophobic, flexible, and lightweight MXene foams for high-performance electromagnetic-interference shielding, Adv. Mater. 29 (28) (2017) 1702367.
[21] F. Shahzad, M. Alhabeb, C.B. Hatter, B. Anasori, S.M. Hong, C.M. Koo, Y. Gogotsi, Electromagnetic interference shielding with 2D transition metal carbides (MXenes), Science 353 (6304) (2016) 1137–1140.
[22] M. Seredych, C.E. Shuck, D. Pinto, M. Alhabeb, E. Precetti, G. Deysher, B. Anasori, N. Kurra, Y. Gogotsi, High-temperature behavior and surface chemistry of carbide MXenes studied by thermal analysis, Chem. Mater. 31 (9) (2019) 3324–3332.
[23] J. Lei, X. Zhang, Z. Zhou, Recent advances in MXene: preparation, properties, and applications, Frontiers of Physics 10 (3) (2015) 276–286.
[24] B. Anasori, M.R. Lukatskaya, Y. Gogotsi, 2D metal carbides and nitrides (MXenes) for energy storage, Nature Reviews Materials 2 (2) (2017) 16098.
[25] M. Han, C.E. Shuck, R. Rakhmanov, D. Parchment, B. Anasori, C.M. Koo, G. Freidman, Y. Gogotsi, Beyond $Ti_3C_2T_X$: MXenes for electromagnetic interference shielding, ACS Nano 14 (4) (2020) 5008–5016.
[26] H.H. Hwu, J.G. Chen, Surface chemistry of transition metal carbides, Chem. Rev. 105 (1) (2005) 185–212.
[27] Y. Zhong, X. Xia, F. Shi, J. Zhan, J. Tu, H. Fan, Transition metal carbides and nitrides in energy storage and conversion, Advanced Science 3 (5) (2016) 1500286.
[28] L. Vazhayal, P. Wilson, K. Prabhakaran, Waste to wealth: lightweight, mechanically strong and conductive carbon aerogels from waste tissue paper for electromagnetic shielding and CO_2 adsorption, Chem. Eng. J. 381 (2020) 122628.
[29] S.J. Park, J.Y. Park, J.W. Chung, H.K. Yang, B.K. Moon, S.S. Yi, Color tunable carbon quantum dots from wasted paper by different solvents for anti-counterfeiting and fluorescent flexible film, Chem. Eng. J. 383 (2020) 123200.
[30] X. Liu, H. Xu, F. Xie, C. Fasel, X. Yin, R. Riedel, Highly flexible and ultrathin Mo_2C film via in-situ growth on graphene oxide for electromagnetic shielding application, Carbon 163 (2020) 254–264.
[31] X. Liu, Z. Yu, R. Ishikawa, L. Chen, X. Liu, X. Yin, Y. Ikuhara, R. Riedel, Single-source-precursor derived RGO/CNTs-SiCN ceramic nanocomposite with ultra-high electromagnetic shielding effectiveness, Acta Mater. 130 (2017) 83–93.
[32] G. Yilmaz, Structural characterization of glass–ceramics made from fly ash containing SiO_2–Al_2O_3–Fe_2O_3–CaO and analysis by FT-IR–XRD–SEM methods, J. Mol. Struct. 1019 (2012) 37–42.
[33] M. Grundner, J. Halbritter, XPS and AES studies on oxide growth and oxide coatings on niobium, J. Appl. Phys. 51 (1) (1980) 397–405.
[34] Z. Li, Y. Cui, Z. Wu, C. Milligan, L. Zhou, G. Mitchell, B. Xu, E. Shi, J.T. Miller, F.H. Ribeiro, Y. Wu, Reactive metal–support interactions at moderate temperature in two-dimensional niobium-carbide-supported platinum catalysts, Nature Catalysis 1 (5) (2018) 349–355.
[35] W. Lengauer, in: R. Riedel (Ed.), Handbook of Ceramic Hard Materials, Wiley-VCH, Weinheim, Germany, 2000, p. 202.
[36] X. Hong, D.D.L. Chung, Carbon nanofiber mats for electromagnetic interference shielding, Carbon 111 (2017) 529–537.
[37] L.C. Jia, K.Q. Ding, R.J. Ma, H.L. Wang, W.J. Sun, D.X. Yan, B. Li, Z.M. Li, Highly conductive and machine-washable textiles for efficient electromagnetic interference shielding, Adv. Mater. Technol. 4 (2) (2019) 1800503.
[38] K. Hayashida, Y. Matsuoka, Electromagnetic interference shielding properties of polymer-grafted carbon nanotube composites with high electrical resistance, Carbon 85 (2015) 363–371.
[39] M. Zulfequar, A. Kumar, Effect of porosity on electrical conductivity of hot pressed AlN ceramic, Rev. Phys. Appl. 21 (9) (1986) 525–529.
[40] B. Shen, W. Zhai, W. Zheng, Ultrathin flexible graphene film: an excellent thermal conducting material with efficient EMI Shielding, Adv. Funct. Mater. 24 (28) (2014) 4542–4548.
[41] W. Song, M. Cao, M. Lu, S. Bi, C. Wang, J. Liu, J. Yuan, L. Fan, Flexible graphene/polymer composite films in sandwich structures for effective electromagnetic interference shielding, Carbon 66 (2014) 67–76.
[42] M.H. Al-Saleh, U. Sundararaj, Electromagnetic interference shielding mechanisms of CNT/polymer composites, Carbon 47 (7) (2009) 1738–1746.
[43] F.G. Cuevas, J.M. Montes, J. Cintas, P. Urban, Electrical conductivity and porosity relationship in metal foams, J. Porous Mater. 16 (6) (2009) 675–681.
[44] K. Zhu, C. Li, Z. Zhu, Measurement of electrical conductivity of porous titanium and Ti_6Al_4V prepared by the powder metallurgy method, Chin. Phys. Lett. 24 (1) (2007) 187–190.
[45] X. Yin, L. Kong, L. Zhang, L. Cheng, N. Travitzky, P. Greil, Electromagnetic properties of Si-C-N based ceramics and composites, International Materials,

Review 59 (2014) 326–355.
[46] M. Cao, X. Wang, W. Cao, J. Yuan, Ultrathin graphene: electrical properties and highly efficient electromagnetic interference shielding, J. Mater. Chem. C 3 (26) (2015) 6589–6599.
[47] C. Liang, M. Hamidinejad, L. Ma, Z. Wang, C.B. Park, Lightweight and flexible graphene/SiC-nanowires/poly (vinylidene fluoride) composites for electromagnetic interference shielding and thermal management, Carbon 156 (2020) 58–66.
[48] Q. Song, F. Ye, X. Yin, W. Li, H. Li, Y. Liu, K. Li, K. Xie, X. Li, Q. Fu, L. Cheng, L. Zhang, B. Wei, Carbon nanotube–multilayered graphene edge plane core-shell hybrid foams for ultrahigh-performance electromagnetic-interference shielding, Adv. Mater. 29 (31) (2017) 1701583.
[49] Z. Chen, C. Xu, C. Ma, W. Ren, H.M. Cheng, Lightweight and flexible graphene foam composites for high-performance electromagnetic interference shielding, Adv. Mater. 25 (9) (2013) 1296–1300.
[50] X. Liu, X. Yin, L. Kong, Q. Li, Y. Liu, W. Duan, L. Zhang, L. Cheng, Fabrication and electromagnetic interference shielding effectiveness of carbon nanotube reinforced carbon fiber/pyrolytic carbon composites, Carbon 68 (2014) 501–510.
[51] X.Y. Fang, X.X. Yu, H.M. Zheng, H.B. Jin, L. Wang, M.S. Cao, Temperature-and thickness-dependent electrical conductivity of few-layer graphene and graphene nanosheets, Phys. Lett. 379 (37) (2015) 2245–2251.
[52] C. Liu, X. Wang, X. Huang, X. Liao, B. Shi, Absorption and reflection contributions to the high performance of electromagnetic waves shielding materials fabricated by compositing leather matrix with metal nanoparticles, ACS Appl. Mater. Interfaces 10 (16) (2018) 14036–14044.
[53] L. Kong, X. Yin, H. Xu, X. Yuan, T. Wang, Z. Xu, J. Huang, R. Yang, H. Fan, Powerful absorbing and lightweight electromagnetic shielding CNTs/RGO composite, Carbon 145 (2019) 61–66.
[54] B.D. Long, R. Othman, M. Umemoto, H. Zuhailawati, Spark plasma sintering of mechanically alloyed in situ copper–niobium carbide composite, J. Alloys Compd. 505 (2010) 510–515.
[55] Z. Zhao, P. Hui, F. Liu, Y. Xu, L. Zhong, M. Zhao, Fabrication of niobium carbide coating on niobium by interstitial carburization, Int. J. Refract. Metals Hard Mater. 88 (2020) 105187.
[56] C. Ang, L. Snead, K. Benensky, Niobium carbide as a technology demonstrator of ultra-high temperature ceramics for fully ceramic microencapsulated fuels, Int. J. Ceramic Eng. Sci. 1 (2019) 92–102.